ADVANCED MATERIALS

www.advmat.de

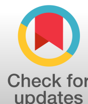

Universal Imaging of Full Strain Tensor in 2D Crystals with Third-Harmonic Generation

*Jing Liang, Jinhuan Wang, Zhihong Zhang, Yingze Su, Yi Guo, Ruixi Qiao, Peizhao Song, Peng Gao, Yun Zhao, Qingze Jiao, Shiwei Wu, Zhipei Sun, Dapeng Yu, and Kaihui Liu**

Quantitatively mapping and monitoring the strain distribution in 2D materials is essential for their physical understanding and function engineering. Optical characterization methods are always appealing due to unique noninvasion and high-throughput advantages. However, all currently available optical spectroscopic techniques have application limitation, e.g., photoluminescence spectroscopy is for direct-bandgap semiconducting materials, Raman spectroscopy is for ones with Raman-active and strain-sensitive phonon modes, and second-harmonic generation spectroscopy is only for noncentrosymmetric ones. Here, a universal methodology to measure the full strain tensor in any 2D crystalline material by polarization-dependent third-harmonic generation is reported. This technique utilizes the third-order nonlinear optical response being a universal property in 2D crystals and the nonlinear susceptibility has a one-to-one correspondence to strain tensor via a photoelastic tensor. The photoelastic tensor of both a noncentrosymmetric D_{3h} WS_2 monolayer and a centrosymmetric D_{3d} WS_2 bilayer is successfully determined, and the strain tensor distribution in homogenously strained and randomly strained monolayer WS_2 is further mapped. In addition, an atlas of photoelastic tensors to monitor the strain distribution in 2D materials belonging to all 32 crystallographic point groups is provided. This universal characterization on strain tensor should facilitate new functionality designs and accelerate device applications in 2D-materials-based electronic, optoelectronic, and photovoltaic devices.

Strain engineering plays a critical role in modern silicon-based semiconductor industry where the strained silicon technology enhances the carrier mobility, reduces the channel size, and postpones the breakdown of Moore's law.[1] In the postsilicon era with channel length shrinking to sub 5 nm, the emergence of 2D materials opens up new possibilities for further miniaturization of electronic devices since their intrinsic thickness is of only ≈1 nm.[2,3] In the future 2D materials–based electronic circuits, strain engineering should play an essential role as well but with much higher regulation capability, because 2D materials can sustain strain up to 10% in comparison to typical 1% in bulk materials.[4–10] For desirable application of strain-engineered 2D materials, it is a prerequisite to quantitatively monitor and map the strain tensor distribution. Optical characterization methods are always appealing for strain measurement due to their superior characteristics of noninvasion and high throughput. Nevertheless, all current prevailing optical spectroscopic methods have their limitation in term of applicable material system. For example, photoluminescence (PL) spectroscopy relies on the luminescent emission of the direct-bandgap semiconductors, while Raman spectroscopy requires the materials to have Raman-active and strain-sensitive phonon modes.[11–16] In addition, both PL and Raman methods are mainly applied to monitor strain amplitude instead of strain tensor. Therefore, a universal optical characterization method to image the full strain tensor in 2D materials is still lacking till now.

Dr. J. Liang, Dr. Z. H. Zhang, Y. Z. Su, Y. Guo, Dr. R. X. Qiao, Dr. P. Z. Song, Prof. P. Gao, Prof. K. H. Liu
State Key Laboratory for Mesoscopic Physics
Collaborative Innovation Center of Quantum Matter
School of Physics
Academy for Advanced Interdisciplinary Studies
Peking University
Beijing 100871, China
E-mail: khliu@pku.edu.cn

Dr. J. H. Wang, Prof. Y. Zhao, Prof. Q. Z. Jiao
School of Chemistry and Chemical Engineering
Beijing Institute of Technology
Beijing 100081, China

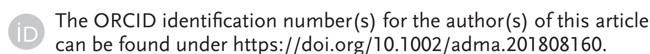
The ORCID identification number(s) for the author(s) of this article can be found under https://doi.org/10.1002/adma.201808160.

Prof. S. W. Wu
State Key Laboratory of Surface Physics
Key Laboratory of Micro and Nano Photonic Structures (MOE) and Department of Physics
Fudan University
Shanghai 200433, China

Prof. Z. P. Sun
Department of Micro- and Nanosciences
Aalto University
Espoo 02150, Finland

Prof. D. P. Yu
Shenzhen Institute for Quantum Science and Engineering and Department of Physics
South University of Science and Technology
Shenzhen 518055, China

DOI: 10.1002/adma.201808160

© 2019 WILEY-VCH Verlag GmbH & Co. KGaA, Weinheim

Fortunately, the rise of nonlinear optical spectroscopy provides easy and fast methods to monitor the strain tensor in 2D materials, as their nonlinear optical response is quite strong even at atomic-layered thickness and their nonlinear optical susceptibility is quantitatively dependent on the crystal lattice structure that directly correlates with the strain tensor.[17–26] Recently, an in situ, noninvasive and sensitive technique based on second-harmonic generation (SHG) has been reported to monitor the strain tensor in noncentrosymmetric 2D materials.[27,28] However, SHG process is forbidden in centrosymmetric 2D materials and cannot be applied to most of the important 2D materials, such as graphene or even-layered transition metal dichalcogenides. In fact, there are higher-order nonlinear optical generations in 2D materials and their signal levels are comparable to SHG[29–41] (it is quite different from bulk materials that the nonlinear signal decreases by orders of magnitude with increasing nonlinear order). Therefore, it is possible to develop new nonlinear optical method to characterize the strain tensor of broader 2D materials than SHG as different-order nonlinear optical processes have different lattice symmetric requirement.

In this work, we report a universal methodology to measure the strain tensor in 2D materials of all kinds of lattice symmetry by polarization-dependent third-harmonic generation (THG). This technique utilizes two distinctive characteristics of third-order nonlinear optical susceptibility, i.e., it is a universal parameter in any 2D crystal different from the second-order nonlinear optical susceptibility, and the susceptibility element is linearly correlated with the strain tensor via a six-rank photoelastic tensor, enabling a simple and direct method for strain measurement. As representative examples, we applied this technique to determine the photoelastic tensor parameters of both noncentrosymmetric (monolayer tungsten disulfide, WS_2) and centrosymmetric 2D material (2H-stacked bilayer WS_2) by their polarization-dependent THG pattern evolution under a series of uniaxial tensile strain. In addition, the full strain tensor mapping is successfully realized in the deformed monolayer WS_2 by solving the strain-tensor-dependent susceptibility equation. We further provide an atlas of photoelastic tensor to describe the strain-tensor-dependent THG intensity for 2D materials belonging to all 32 crystallographic point groups. This full characterization on strain tensor should facilitate new designs and applications in the future electronic, optoelectronic, and photovoltaic devices that are based on a large range of 2D materials with different lattice symmetries.

THG is a third-order nonlinear optical process in which three photons with the frequency ω are combined to generate one photon with tripled frequency of 3ω after interacting with a nonlinear material (**Figure 1**a). In our experiment, under excitation of a linearly polarized ultrafast laser (1288 nm, 100 fs),

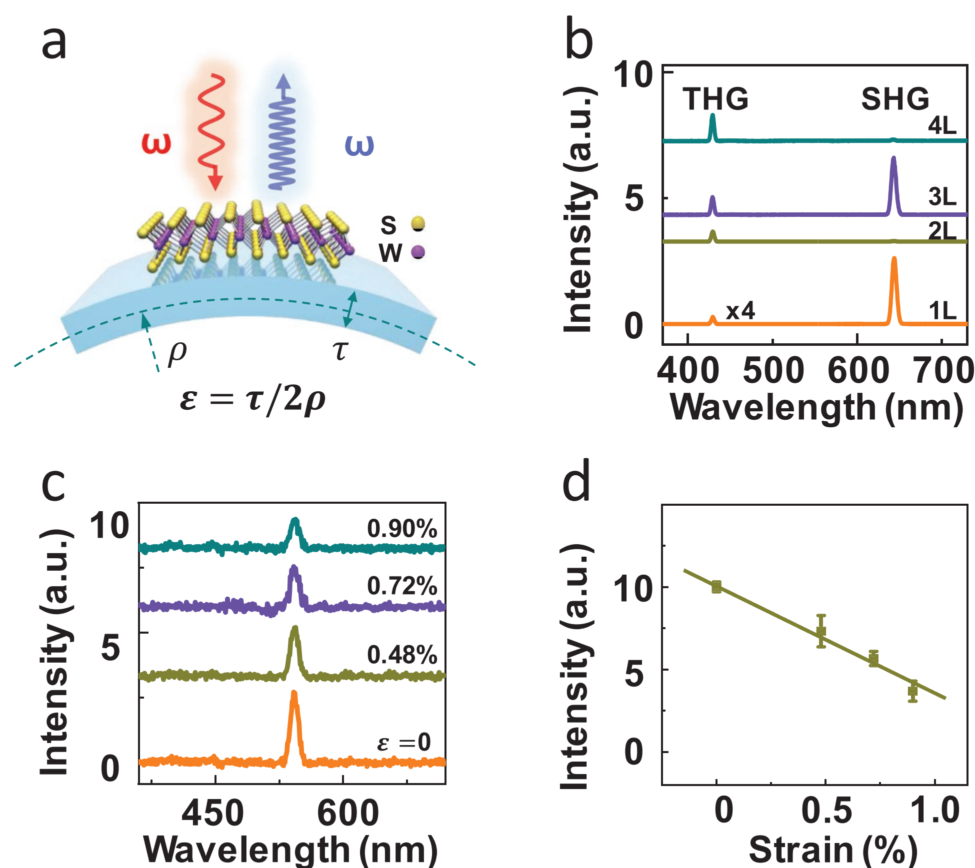

Figure 1. THG response of monolayer WS_2 under strain. a) Schematic diagram of two-point bending configuration and THG process in monolayer WS_2. The supporting substrate is optical transparent flexible Acrylic. The left red and right violet waves indicate excitation beam (ω) and generated THG signal (3ω), respectively. b) SHG and THG spectra of mono- and few-layered WS_2. c) The THG spectral evolution of monolayer WS_2 under uniaxial tensile strain. d) The sensitivity of THG on strain in monolayer WS_2. The error bars represent the standard error from measurements of eight samples.

© 2019 WILEY-VCH Verlag GmbH & Co. KGaA, Weinheim

both of the SHG (644 nm) and THG (429 nm) signals from exfoliated few-layered WS_2 flakes could be collected (Figure 1b). The layer number of WS_2 flakes was verified by both optical and atomic force microscopy images (Figure S1, Supporting Information). As expected, the SHG in centrosymmetric even-layered WS_2 (two or four layers) vanishes to nearly zero. While, the THG in both odd- and even-layered WS_2 (one to four layers) is obviously strong, originating from the fact that the third-order nonlinear optical process is the most universal and intrinsic nonlinear response of any 2D crystal without symmetric constraint. These comparison results confirm that THG has the potential to be a general method to measure the strain in 2D materials.

To verify the feasibility in monitoring the strain by THG, the optical spectra from monolayer WS_2 flakes under a series of uniaxial tensile strain were collected (Figure 1c). In the experiment, the chemical vapor deposition (CVD) grown atomic-layered WS_2 flakes were transferred on the flexible Acrylic substrate (see the Experimental Section for details). The layer number of WS_2 flakes was verified by both optical images and Raman/PL spectroscopy (Figure S2a,b, Supporting Information).[16,42] The uniaxial tensile strain was applied to WS_2 by bending the flexible Acrylic substrate (Figure 1a). The magnitude of strain could be directly calculated by the geometric construction ($\varepsilon = \tau/2\rho$, $\tau = 0.5$ mm is the substrate thickness, and ρ is the curvature radius of the neutral plane) or the red-shift of PL peak position (Figure S2c, Supporting Information, –100 meV per % strain).[16] It is observed that the THG intensity of monolayer WS_2 decreases rapidly with increasing strain (Figure 1c). Detailed analysis (Figure 1d) indicates that the relative change of THG intensity ($\frac{\Delta I_\varepsilon}{I_0} = \frac{I_\varepsilon - I_0}{I_0} = -0.65/\%\varepsilon$, I_ε and I_0, respectively, stand for THG intensity in strain and strain-free cases) is more than one order of magnitude larger than that of PL peak energy ($\frac{\Delta E_\varepsilon}{E_0} = \frac{E_\varepsilon - E_0}{E_0} = -0.05/\%\varepsilon$, E_ε and E_0, respectively, stand for the PL peak energy with and without strain) under the same strain. The high strain sensitivity provides the foundation of THG to serve as an effective method to measure the strain tensor. In the following experiment, monolayer (D_{3h}) and 2H-stacked bilayer WS_2 (D_{3d}) were chosen as representative examples to illustrate the universality of THG method in determining strain tensor in both noncentrosymmetric and centrosymmetric material systems.

In this experiment, we carried out polarization-dependent THG measurement and monitor the pattern evolution in noncentrosymmetric monolayer WS_2 under a series of uniaxial tensile strain (**Figure 2**). The incident laser is polarized and the generated THG with polarization parallel ($I_\parallel$) and perpendicular ($I_\perp$) to the incident polarization was measured. The intrinsic THG response of strain-free monolayer WS_2 is independent of incident polarization θ: $I_\parallel = I_0$, $I_\perp = 0$, consistent with the symmetry analysis of the third-order nonlinear susceptibility in D_{3h} materials (Note S1, Supporting Information).

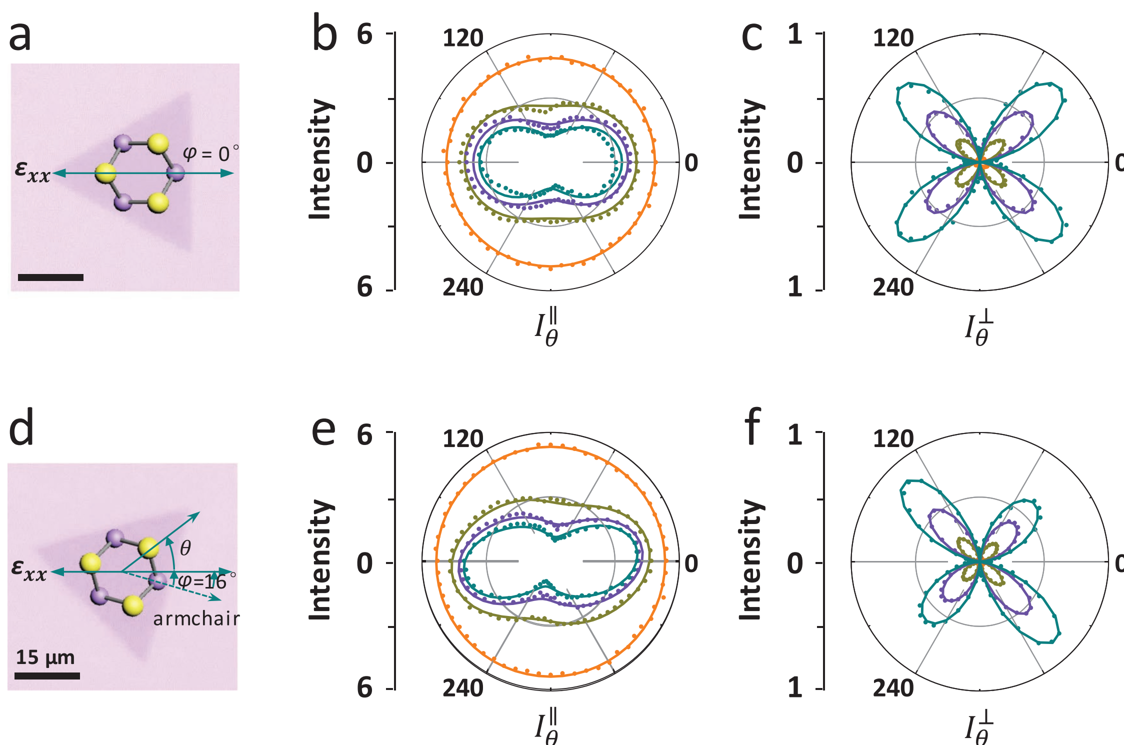

Figure 2. Polarization-dependent THG pattern evolution of monolayer WS_2 under uniaxial tensile strain. a) Optical images of monolayer WS_2 and the corresponding crystal lattice structure by a ball-stick model. The uniaxial tensile strain ε_{xx} is fixed along horizontal direction with a relative angle ($\varphi = 0°$) to the armchair direction of WS_2. b,c) θ-dependent parallel $I_\theta^\parallel$ (b) or perpendicular $I_\theta^\perp$ (c) component of THG from the monolayer WS_2 in (a) under a series of uniaxial tensile strains. θ is the laser polarization from the horizontal direction. Dots are original data and lines are theoretical fits. The orange, dark yellow, violet, and dark cyan colors represent strain magnitudes of 0%, 0.48%, 0.72%, and 0.90%, respectively. d–f) THG response of another monolayer WS_2 with a general relative angle ($\varphi = 16°$) to the armchair direction of WS_2. All other experimental conditions are the same as in (a–c).

© 2019 WILEY-VCH Verlag GmbH & Co. KGaA, Weinheim

Meanwhile, the THG pattern under strain shows obvious strain-tensor dependence. When the uniaxial tensile strain is along WS_2 armchair direction (Figure 2a, $\varphi = 0°$, φ is the angle of horizontal strain direction from WS_2 armchair direction), the $I_{\parallel}$ ($I_{\perp}$) intensity decreases (increases) gradually with increasing strain magnitude. The $I_{\parallel}$ pattern evolves into symmetric dumbbell pattern (Figure 2b) and $I_{\perp}$ stretches out to four equal-sized petals (Figure 2c). When the uniaxial tensile strain is along a general WS_2 lattice direction (Figure 2d, $\varphi = 16°$), the $I_{\parallel}$ pattern evolves into asymmetric dumbbell pattern (Figure 2e) and $I_{\perp}$ stretches out to four asymmetry petals as well (Figure 2f). The qualitative understanding on the relation between THG pattern and the strain can be obtained from the symmetric evaluation. Uniaxial tensile strain breaks the threefold rotational symmetry of WS_2 lattice and leads to the anisotropic $I_{\parallel}$ and $I_{\perp}$ pattern evolution. In addition, the strain direction has a direct correspondence with the major axis of $I_{\parallel}$. The special $\varphi = 0°$ (general $\varphi = 16°$) strain conserves (breaks) the mirror plane normal to armchair direction and results in mirror-symmetric (asymmetric) $I_{\parallel}$ and $I_{\perp}$ patterns. Therefore, the distortion of $I_{\parallel}$ and $I_{\perp}$ pattern directly denotes the strain orientation from the WS_2 armchair direction. The detailed pattern evolution feature contains the information of both strain amplitude and direction, and the quantitative description on the relation between THG pattern and strain tensor will be given in the latter theoretical section.

To demonstrate the universality of THG to monitor strain tensor, we investigated the polarization-dependent THG pattern evolution in centrosymmetric 2H-stacked bilayer WS_2 flakes under a series of uniaxial tensile strain (**Figure 3**). It is worth noting that PL and SHG methods are challenging to measure the strain in the 2H-stacked WS_2 flakes due to their extremely weak PL and forbidden SHG. Our THG imaging results are shown in Figure 3. In strain-free case, 2H-stacked bilayer WS_2 gives the same isotropic THG patterns as monolayer due to maintained threefold rotational symmetry. While the THG intensity is roughly quadrupled because the depletion of the fundamental light and the phase mismatch could be ignored in the THG process in few-layered 2D configuration and the THG intensity is only determined by the thickness of 2D materials. Under uniaxial strain (Figure 3a, $\varphi = 24°$), $I_{\parallel}$ shrinks into a parallelogram (Figure 3b) and $I_{\perp}$ stretches out to asymmetric four petals (Figure 3c).

The THG pattern evolution under strain is similar to that in monolayer WS_2 due to the same symmetry breaking of threefold rotation symmetry and mirror symmetry along armchair direction. But the ellipticity of $I_{\parallel}$ pattern is smaller than that in monolayer case because the nonlinear susceptibility of bilayer WS_2 has a relative lower strain sensitivity. Nevertheless, here we demonstrate the advantage of using THG for strain measurement in centrosymmetric 2H-stacked bilayer WS_2 which is challenging to achieve with SHG due to that SHG is forbidden in these materials with inversion symmetry. The detailed pattern evolution description in 2H-stacked bilayer WS_2 will be given in the below theoretical part.

Polarization-dependent THG carries the information of lattice symmetry by the third-order nonlinear susceptibility tensor $\chi^{(3)}_{ijkl}$. Strain deforms the crystal lattice, breaks the crystal symmetry, changes $\chi^{(3)}_{ijkl}$, and eventually determines the polarization-dependent THG pattern. The strain regulation on the polarization-dependent THG pattern is determined by the linear response of $\chi^{(3)}_{ijkl}$ to the strain tensor u_{mn} in the form of

$$\chi^{(3)}_{ijkl} = \chi^{(3,0)}_{ijkl} + p_{ijklmn} u_{mn} \tag{1}$$

where $p_{ijklmn} = \frac{\partial \chi^{(3,0)}_{ijkl}}{\partial u_{mn}}$ is a sixth-rank photoelastic tensor, $\chi^{(3,0)}_{ijkl}$ and $\chi^{(3)}_{ijkl}$ are, respectively, the third-order nonlinear susceptibility under strain-free and strain conditions. u_{mn} has different representations in different coordinate systems. Here, we choose the principal strain coordinates (x, y), in which shear components vanish

$$u_{mn} = \begin{pmatrix} \varepsilon_{xx} - \nu\varepsilon_{yy} & 0 \\ 0 & \varepsilon_{yy} - \nu\varepsilon_{xx} \end{pmatrix} \tag{2}$$

Here ν is the Poisson's ratio of a crystal, x and y denotes the ε_{xx} and ε_{yy} orientation and x-axis has an angle α from the horizontal direction. Equation (1) can be expressed in the lab coordinates (X, Y) by strain transformation formula, where X and Y stand for horizontal and vertical direction, respectively (Note S2, Supporting Information).

Considering the symmetry of third-order nonlinear susceptibility in THG process, the symmetry of strain tensor, and point-group-dependent symmetry operations, the photoelastic tensor p_{ijklmn} could be represented compactly by several irrelevant

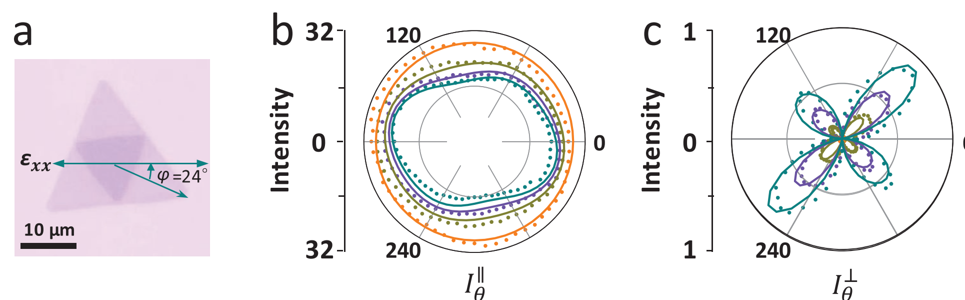

Figure 3. Polarization-dependent THG pattern evolution of 2H-stacked bilayer WS_2 under uniaxial tensile strain. a) Optical image of 2H-stacked WS_2 bilayer. The uniaxial tensile strain ε_{xx} has a relative angle ($\varphi = 24°$) to the armchair direction of WS_2. b,c) θ-dependent parallel $I_\theta^{\parallel}$ (b) or perpendicular $I_\theta^{\perp}$ (c) component of THG from bilayer WS_2 under a series of uniaxial tensile strains. The orange, dark yellow, violet, and dark cyan colors represent strain magnitudes of 0%, 0.48%, 0.72%, and 0.90%, respectively.

© 2019 WILEY-VCH Verlag GmbH & Co. KGaA, Weinheim

Table 1. Photoelastic tensor p_{ijklmn} of WS_2 (D_{3h} or D_{3d}).

i	*jkl mn*	*aaa*	*aab/aba/baa*	*abb/bab/bba*	*bbb*
a	***aa***	$\frac{-k_1+3k_2+3k_3+3k_4}{4}$	0	$\frac{k_1+k_2-3k_3+k_4}{4}$	0
	ab/ba	0	$\frac{-k_1-5k_2-k_3+3k_4}{8}$	0	$\frac{-3k_1+9k_2-3k_3+k_4}{8}$
	bb	k_1	0	k_3	0
b	***aa***	0	$\frac{k_1-3k_2+k_3+k_4}{4}$	0	$\frac{3k_1+3k_2+3k_3-k_4}{4}$
	ab/ba	$\frac{-k_1+3k_2-9k_3+3k_4}{8}$	0	$\frac{-3k_1+k_2+5k_3+k_4}{8}$	0
	bb	0	k_2	0	k_4

In 2D configuration, every index in p_{ijklmn} has two degrees of freedom: *a* and *b* (armchair and zigzag direction of WS_2). k_1, k_2, k_3, and k_4 are four photoelastic tensor parameters, which determine the photoelastic tensor p_{ijklmn}.

photoelastic tensor parameters (Note S3, Table S1, Supporting Information). For the specific D_{3h} monolayer WS_2 and D_{3d} 2H-stacked bilayer WS_2, their photoelastic tensors both have 32 nonzero elements and are determined by only four independent photoelastic tensor parameters (k_1, k_2, k_3, k_4) expressed in the crystal coordinates (*a*, *b*); *a* and *b* denote the armchair and zigzag direction of WS_2 and φ is the angle of *X*-axis away from *a*-axis (**Table 1**). After rotating the strain tensor and the photoelastic tensor into the lab coordinates (*X, Y*) (Note S2, Supporting Information), the polarization-dependent THG of strained atomic-layered WS_2 could be deduced from Equation (1) as

$$I_{\parallel} = \left[\chi^{(3,0)} + 3(1-\nu)(\varepsilon_{xx}+\varepsilon_{yy})A + (1+\nu)(\varepsilon_{yy}-\varepsilon_{xx})\left(4B\cos(2\theta-2\alpha)+C\cos(6\varphi+4\theta+2\alpha)\right)\right]^2$$
$$I_{\perp} = \left[(1+\nu)(\varepsilon_{yy}-\varepsilon_{xx})\left(2D\sin(2\theta-2\alpha)+C\sin(6\varphi+4\theta+2\alpha)\right)\right]^2 \quad (3)$$

where $A = k_1 + k_2 + k_3 + k_4$, $B = k_1 - k_4$, $C = k_1 - 3k_2 - 3k_3 + k_4$, and $D = k_1 - 3k_2 + 3k_3 - k_4$. Therefore, the strain regulation on the polarization-dependent THG pattern can be quantitatively described by the four photoelastic tensor parameters k_1, k_2, k_3, and k_4.

By fitting the polarization-dependent THG pattern $I_{\parallel}$ and $I_{\perp}$ under a series of uniaxial tensile strain at the same time (lines in Figures 2 and 3) with Equation (3), we can extract the photoelastic tensor parameters of monolayer as well as 2H-stacked bilayer WS_2 as shown in **Table 2**. During the theoretical fitting process, $\varepsilon_{yy} = 0$ due to uniaxial strain, $\alpha = 0$ due to the fixed ε_{xx} along horizontal direction, Poisson's ratio of $\nu = 0.22$, and the intrinsic third-order nonlinear susceptibility $\chi^{(3,0)} = 2.4 \times 10^{-19}$ $m^2\ V^{-2}$ of WS_2 are used.[43,44] It is obviously proved that the strain tensor information can be quantitatively determined by the polarization-dependent THG patterns.

In the following, we will illustrate the application of our method to map the full strain tensor under the general conditions rather than uniaxial strain. The general strain tensor can be described in simplified form of (ε_{xx}, ε_{yy}, α). The polarization-dependent THG pattern contains the full information of principal strain (magnitude of ε_{xx} and ε_{yy} and orientation α) and one can fit out all these three parameters unambiguously by Equation (3).

We first provide a convincing test on imaging the uniform uniaxial strain tensor (ε_{xx}, 0, 0°) distribution in a known homogenously tensile-strained monolayer WS_2 membrane. In the same way, the uniaxial tensile strain along the horizontal direction was applied on monolayer WS_2 by bending the flexible substrate and the magnitude is determined to be 0.72% from the geometrical bending (**Figure 4**a). The full strain tensor at a representative point is determined to be (0.77%, 0.07%, 0.3°) by the THG pattern fitting (Figure 4b). A strain tensor map is then recorded and the resulting principal strain tensors described by ε_{xx} and ε_{yy} are plotted as vectors in Figure 4c,d, respectively. The uniform magnitude of ε_{xx} (0.72 ± 0.05%) as well as nearly zero ε_{yy} and α denotes the presence of uniaxial strain along the horizontal direction.

Further, we demonstrate its application on mapping the inhomogenous strain tensor distribution in monolayer WS_2 membrane which is naturally formed during the rapid drying process after the transfer process (Figure 4e). The strain tensor at a point marked in Figure 4e was determined to be (0.30%, 0.01%, 20°) (Figure 4f). The full strain tensor field is mapped

Table 2. Photoelastic tensor parameters of $WS_2(\times\chi^{(3,0)})$.

	k_1	k_2	k_3	k_4
Monolayer	−7.66	−5.86	1.46	−3.60
Bilayer	−3.50	−2.00	0.79	−2.16

 © 2019 WILEY-VCH Verlag GmbH & Co. KGaA, Weinheim

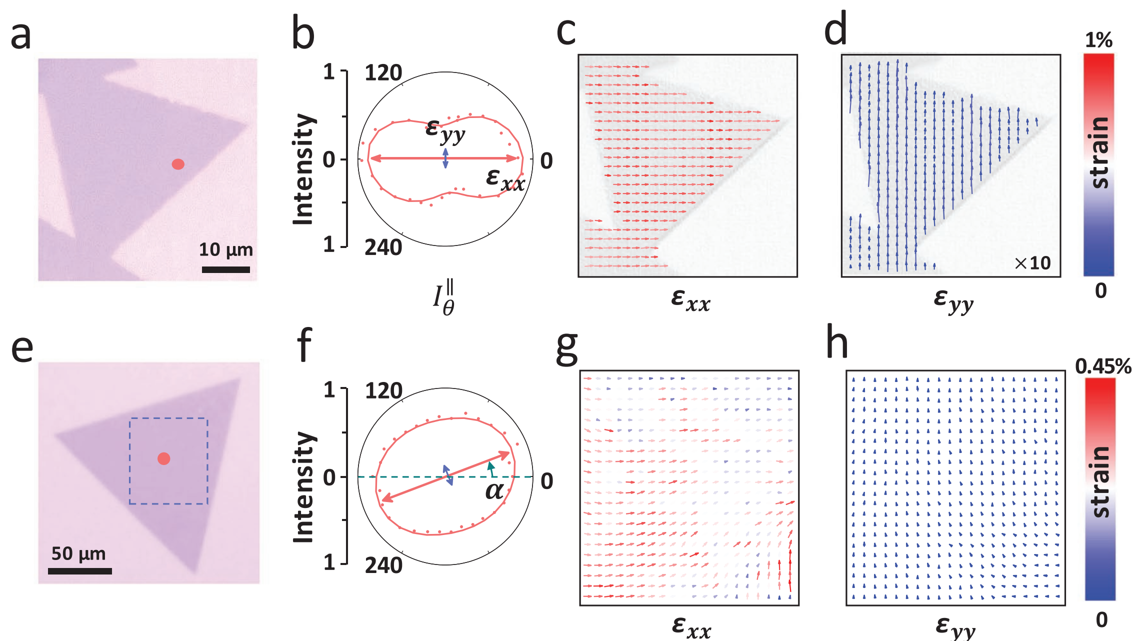

Figure 4. Full strain tensor mapping on monolayer WS_2 membrane. a) Optical image of a monolayer WS_2 under a controlled uniaxial tensile strain. b) The polarization-dependent THG pattern of monolayer WS_2 at the local point indicated in (a). ε_{xx} and ε_{yy} components of the principal strain tensor are indicated by red and blue double-headed arrows, respectively. c,d) The distribution of ε_{xx} (c) and ε_{yy} (d), indicated by arrows, of the principal strain tensor in a uniaxial tensile-strained monolayer WS_2. The color and length of the arrows indicate the magnitude of the strain component while the orientation denotes the direction of corresponding strain components. e–h) The optical image (e), representative local strain tensor (f), and principal strain tensor distribution (g,h) in an inhomogenous strained monolayer WS_2 membrane indicated in the dashed rectangle in (e).

(Figure 4g,h) and we conclude that only tensile strain is present in this monolayer WS_2 film since all strain values are positive, which is consistent with the fact that the membrane spreads smoothly on the substrate without wrinkles. We also successfully measure the inhomogenous strain tensor distribution of a WS_2 monolayer membrane suspended on a transmission electron microscopy hole grid (Figure S3, Supporting Information).

In our experiment, we demonstrate the application of polarization-dependent THG to monitor the full strain tensor in centrosymmetric D_{3h} and noncentrosymmetric D_{3d} crystal materials. The THG-based strain tensor measurement still functions well regardless of the doping level of the 2D materials (Figures S4 and S5, Supporting Information), and it has higher spatial resolution compared to SHG due to higher-order excitation power dependence. Most importantly, the THG-based strain tensor measurement is in principle applicable to all 2D crystal materials of any kind of crystallographic point groups. We tested the strain-induced THG pattern evolution in another material of monolayer MoS_2 and the method works well (Figure S6, Supporting Information). Furthermore, we provide an atlas of six-rank photoelastic tensor tables of all 32 crystallographic point groups for strain tensor determination (Tables S2–S13, Supporting Information), which acts as a looking-up table for strain tensor determination in 2D crystals by THG. It is seen that, the strain-tensor-dependent THG is only determined by several free parameters of photoelastic tensor. Once these parameters are known, the quantitative principal strain tensor mapping can be extracted by polarization-dependent THG in a noninvasive and high-throughput way. Surely, the predetermination of these free parameters in the atlas for different 2D materials is needed and should be done in the future either by experiment or theory.[45,46]

In summary, we report a universal methodology based on polarization-dependent THG to image strain tensor distribution in 2D crystalline materials. The universality of the method is verified by the strain measurement in both noncentrosymmetric monolayer and centrosymmetric 2H-stacked bilayer WS_2. On the basis of experimental results and theoretical analysis, we extract the numerical value of photoelastic tensor parameters which quantitatively describes the strain regulation on the third-order nonlinear susceptibility. With such photoelastic tensor parameters, one can conveniently determine the strain distribution from the polarization-dependent THG pattern. Our methodology expands the application of third-order nonlinear process of THG to strain tensor characterization and should promote new functionality designs and accelerate device applications in 2D materials–based electronic, optoelectronic, and photovoltaic devices. Without the constraint of crystal symmetry, the THG methodology is in principle applicable to any 2D crystalline materials.

Experimental Section

Growth of Monolayer and Bilayer WS_2: WS_2 on SiO_2/Si substrate was grown by CVD method by using WO_3 and S powder as precursors. WO_3 powder (10.0 mg) and NaCl powder (1.5 mg) was placed in quartz boat at the center of the tube furnace. S powder (30.0 mg) was placed on the upstream side while the substrate was upon the quartz boat at the downstream side. The growth was performed under ambient pressure Ar gas. The procedure was as follows: kept at 105 °C with 500 sccm Ar

© 2019 WILEY-VCH Verlag GmbH & Co. KGaA, Weinheim

flow for 1 h, ramped to 800 °C with 15 sccm Ar flow in 50 min, kept at 800 °C with 250 sccm Ar flow for 10 min, and then naturally cooled down to room temperature.

Sample Preparation on Flexible Substrate: 9% poly(methyl methacrylate) (PMMA), 950 K) in anisole solution was spin-coated onto SiO_2/Si substrates with WS_2 flakes and baked at 180 °C for 2 min. Then the sample was immersed into KOH solution (0.1 M) at 80 °C for 5 min. After being lifted off from the original substrate, the PMMA/WS_2 flakes were thoroughly washed with deionized water and then transferred to the target flexible Acrylic substrate. The PMMA/WS_2/Acrylic was dried and baked at 60 °C for 10 min to ensure the strong interaction between WS_2 and Acrylic.

Optical Characterization of WS_2: Microscopy images of WS_2 flakes on Acrylic were taken by Olympus microscope (Olympus BX51). PL and Raman spectra are probed by home-built confocal microscope system with laser excitation wavelength of 532 nm and average power of 200 μW.

Experimental THG Setup: Femtosecond pulses (≈100 fs, 80 MHz) at 1288 nm were generated by a Ti:sapphire oscillator (Spectra-Physics Mai Tai laser) equipped with an optical parametric oscillator. The excitation beam was normally incident and its linear polarization was controlled by a half-wave plate in front of the objective (40×, N.A. = 0.65). In reflection geometry, a linear analyzer parallel (perpendicular) to the incident polarization was utilized to extract the parallel (perpendicular) component $I_{\parallel}$ ($I_{\perp}$) of THG from the sample. The signal was recorded by a grating spectrograph with CCD (Princeton SP-2500i).

Supporting Information

Supporting Information is available from the Wiley Online Library or from the author.

Acknowledgements

This work was supported by National Key R&D Program of China (2016YFA0300903 and 2016YFA0300804), NSFC (51522201 and 11474006), National Equipment Program of China (ZDYZ2015-1), Beijing Graphene Innovation Program (Z161100002116028), Science, Technology and Innovation Commission of Shenzhen Municipality (ZDSYS20170303165926217 and JCYJ20170412152620376), Guangdong Innovative and Entrepreneurial Research Team Program (2016ZT06D348), and the National Program for Thousand Young Talents of China.

Conflict of Interest

The authors declare no conflict of interest.

Keywords

2D materials, photoelastic tensor, strain tensor characterization, third-harmonic generation

Received: December 19, 2018
Revised: March 2, 2019
Published online:

[1] R. S. Jacobsen, K. N. Andersen, P. I. Borel, J. Fage-Pedersen, L. H. Frandsen, O. Hansen, M. Kristensen, A. V. Lavrinenko, G. Moulin, H. Ou, C. Peucheret, B. Zsigri, A. Bjarklev, *Nature* **2006**, *441*, 199.
[2] Q. H. Wang, K. Kalantar-Zadeh, A. Kis, J. N. Coleman, M. S. Strano, *Nat. Nanotechnol.* **2012**, *7*, 699.
[3] G. Iannaccone, F. Bonaccorso, L. Colombo, G. Fiori, *Nat. Nanotechnol.* **2018**, *13*, 183.
[4] C. Lee, X. D. Wei, J. W. Kysar, J. Hone, *Science* **2008**, *321*, 385.
[5] N. Levy, S. A. Burke, K. L. Meaker, M. Panlasigui, A. Zettl, F. Guinea, A. H. C. Neto, M. F. Crommie, *Science* **2010**, *329*, 544.
[6] J. Feng, X. F. Qian, C. W. Huang, J. Li, *Nat. Photonics* **2012**, *6*, 866.
[7] H. Y. Yu, G. B. Liu, P. Gong, X. D. Xu, W. Yao, *Nat. Commun.* **2014**, *5*, 3876.
[8] W. B. Li, J. Li, *Nat. Commun.* **2016**, *7*, 10843.
[9] J. Lee, Z. F. Wang, H. C. Xie, K. F. Mak, J. Shan, *Nat. Mater.* **2017**, *16*, 887.
[10] Y. P. Liu, J. N. B. Rodrigues, Y. Z. Luo, L. J. Li, A. Carvalho, M. Yang, E. Laksono, J. P. Lu, Y. Bao, H. Xu, S. J. R. Tan, Z. Z. Qiu, C. H. Sow, Y. P. Feng, A. H. C. Neto, S. Adam, J. Lu, K. P. Loh, *Nat. Nanotechnol.* **2018**, *13*, 828.
[11] Y. Y. Hui, X. F. Liu, W. J. Jie, N. Y. Chan, J. H. Hao, Y. T. Hsu, L. J. Li, W. L. Guo, S. P. Lau, *ACS Nano* **2013**, *7*, 7126.
[12] K. He, C. Poole, K. F. Mak, J. Shan, *Nano Lett.* **2013**, *13*, 2931.
[13] H. J. Conley, B. Wang, J. I. Ziegler, R. F. Haglund, S. T. Pantelides, K. I. Bolotin, *Nano Lett.* **2013**, *13*, 3626.
[14] A. Castellanos-Gomez, R. Roldan, E. Cappelluti, M. Buscema, F. Guinea, H. S. J. van der Zant, G. A. Steele, *Nano Lett.* **2013**, *13*, 5361.
[15] Y. L. Wang, C. X. Cong, C. Y. Qiu, T. Yu, *Small* **2013**, *9*, 2857.
[16] X. He, H. Li, Z. Y. Zhu, Z. Y. Dai, Y. Yang, P. Yang, Q. Zhang, P. Li, U. Schwingenschlogl, X. X. Zhang, *Appl. Phys. Lett.* **2016**, *109*, 173105.
[17] Y. L. Li, Y. Rao, K. F. Mak, Y. M. You, S. Y. Wang, C. R. Dean, T. F. Heinz, *Nano Lett.* **2013**, *13*, 3329.
[18] X. B. Yin, Z. L. Ye, D. A. Chenet, Y. Ye, K. O'Brien, J. C. Hone, X. Zhang, *Science* **2014**, *344*, 488.
[19] W. T. Hsu, Z. A. Zhao, L. J. Li, C. H. Chen, M. H. Chiu, P. S. Chang, Y. C. Chou, W. H. Chang, *ACS Nano* **2014**, *8*, 2951.
[20] K. L. Seyler, J. R. Schaibley, P. Gong, P. Rivera, A. M. Jones, S. F. Wu, J. Q. Yan, D. G. Mandrus, W. Yao, X. D. Xu, *Nat. Nanotechnol.* **2015**, *10*, 407.
[21] J. X. Cheng, T. Jiang, Q. Q. Ji, Y. Zhang, Z. M. Li, Y. W. Shan, Y. F. Zhang, X. G. Gong, W. T. Liu, S. W. Wu, *Adv. Mater.* **2015**, *27*, 4069.
[22] E. Mishina, N. Sherstyuk, S. Lavrov, A. Sigov, A. Mitioglu, S. Anghel, L. Kulyuk, *Appl. Phys. Lett.* **2015**, *106*, 131901.
[23] M. Zhao, Z. L. Ye, R. Suzuki, Y. Ye, H. Y. Zhu, J. Xiao, Y. Wang, Y. Iwasa, X. Zhang, *Light: Sci. Appl.* **2016**, *5*, e16131.
[24] A. Saynatjoki, L. Karvonen, H. Rostami, A. Autere, S. Mehravar, A. Lombardo, R. A. Norwood, T. Hasan, N. Peyghambarian, H. Lipsanen, K. Kieu, A. C. Ferrari, M. Polini, Z. P. Sun, *Nat. Commun.* **2017**, *8*, 893.
[25] X. L. Wen, W. G. Xu, W. J. Zhao, J. B. Khurgin, Q. H. Xiong, *Nano Lett.* **2018**, *18*, 1686.
[26] A. Autere, H. Jussila, Y. Y. Dai, Y. D. Wang, H. Lipsanen, Z. P. Sun, *Adv. Mater.* **2018**, *30*, 1705963.
[27] J. Liang, J. Zhang, Z. Z. Li, H. Hong, J. H. Wang, Z. H. Zhang, X. Zhou, R. X. Qiao, J. Y. Xu, P. Gao, Z. R. Liu, Z. F. Liu, Z. P. Sun, S. Meng, K. H. Liu, D. P. Yu, *Nano Lett.* **2017**, *17*, 7539.
[28] L. Mennel, M. M. Furchi, S. Wachter, M. Paur, D. K. Polyushkin, T. Mueller, *Nat. Commun.* **2018**, *9*, 516.
[29] E. Hendry, P. J. Hale, J. Moger, A. K. Savchenko, S. A. Mikhailov, *Phys. Rev. Lett.* **2010**, *105*, 097401.
[30] S. Y. Hong, J. I. Dadap, N. Petrone, P. C. Yeh, J. Hone, R. M. Osgood, *Phys. Rev. X* **2013**, *3*, 021014.
[31] R. Wang, H. C. Chien, J. Kumar, N. Kumar, H. Y. Chiu, H. Zhao, *ACS Appl. Mater. Interfaces* **2014**, *6*, 314.

© 2019 WILEY-VCH Verlag GmbH & Co. KGaA, Weinheim

[32] C. Torres-Torres, N. Perea-Lopez, A. L. Elias, H. R. Gutierrez, D. A. Cullen, A. Berkdemir, F. Lopez-Urias, H. Terrones, M. Terrones, *2D Mater.* **2016**, *3*, 021005.
[33] S. Bikorimana, P. Lama, A. Walser, R. Dorsinville, S. Anghel, A. Mitioglu, A. Micu, L. Kulyuk, *Opt. Express* **2016**, *24*, 20685.
[34] M. J. L. F. Rodrigues, C. J. S. de Matos, Y. W. Ho, H. Peixoto, R. E. P. de Oliveira, H. Y. Wu, A. H. C. Neto, J. Viana-Gomes, *Adv. Mater.* **2016**, *28*, 10693.
[35] N. Yoshikawa, T. Tamaya, K. Tanaka, *Science* **2017**, *356*, 736.
[36] H. Z. Liu, Y. L. Li, Y. S. You, S. Ghimire, T. F. Heinz, D. A. Reis, *Nat. Phys.* **2017**, *13*, 262.
[37] N. Youngblood, R. M. Peng, A. Nemilentsau, T. Low, M. Li, *ACS Photonics* **2017**, *4*, 8.
[38] R. I. Woodward, R. T. Murray, C. F. Phelan, R. E. P. de Oliveira, T. H. Runcorn, E. J. R. Kelleher, S. Li, E. C. de Oliveira, G. J. M. Fechine, G. Eda, C. J. S. de Matos, *2D Mater.* **2017**, *4*, 011006.
[39] R. E. F. Silva, I. V. Blinov, A. N. Rubtsov, O. Smirnova, M. Ivanov, *Nat. Photonics* **2018**, *12*, 266.
[40] T. Jiang, D. Huang, J. L. Cheng, X. D. Fan, Z. H. Zhang, Y. W. Shan, Y. F. Yi, Y. Y. Dai, L. Shi, K. H. Liu, C. G. Zeng, J. Zi, J. E. Sipe, Y. R. Shen, W. T. Liu, S. W. Wu, *Nat. Photonics* **2018**, *12*, 430.
[41] G. Soavi, G. Wang, H. Rostami, D. G. Purdie, D. De Fazio, T. Ma, B. R. Luo, J. J. Wang, A. K. Ott, D. Yoon, S. A. Bourelle, J. E. Muench, I. Goykhman, S. Dal Conte, M. Celebrano, A. Tomadin, M. Polini, G. Cerullo, A. C. Ferrari, *Nat. Nanotechnol.* **2018**, *13*, 583.
[42] W. J. Zhao, Z. Ghorannevis, K. K. Amara, J. R. Pang, M. Toh, X. Zhang, C. Kloc, P. H. Tan, G. Eda, *Nanoscale* **2013**, *5*, 9677.
[43] K. Liu, Q. M. Yan, M. Chen, W. Fan, Y. H. Sun, J. Suh, D. Y. Fu, S. Lee, J. Zhou, S. Tongay, J. Ji, J. B. Neaton, J. Q. Wu, *Nano Lett.* **2014**, *14*, 5097.
[44] Z. P. Sun, A. Martinez, F. Wang, *Nat. Photonics* **2016**, *10*, 227.
[45] J. L. Cheng, N. Vermeulen, J. E. Sipe, *New J. Phys.* **2014**, *16*, 053014.
[46] S. Khorasani, *Commun. Theor. Phys.* **2018**, *70*, 344.

© 2019 WILEY-VCH Verlag GmbH & Co. KGaA, Weinheim